

Planetesimal formation via the streaming instability with multiple grain sizes

J. J. Rucska,¹ J. W. Wadsley¹★

¹*Department of Physics and Astronomy, McMaster University, Hamilton, L8S 4M1, Canada*

Accepted XXX. Received YYY; in original form ZZZ

ABSTRACT

Kilometre-sized planetesimals form from pebbles of a range of sizes. We present the first simulations of the streaming instability that begin with a realistic, peaked size distribution, as expected from grain growth predictions. Our 3D numerical simulations directly form planetesimals via the gravitational collapse of pebble clouds. Models with multiple grain sizes show spatially distinct dust populations. The smallest grains in the size distribution do not participate in the formation of filaments or the planetesimals that are formed by the remaining ~80% of the dust mass. This implies a size cutoff for pebbles incorporated into asteroids and comets. Observations cannot resolve this dust clumping. However, we show that clumping, combined with optical depth effects, can cause significant underestimates of the dust mass, with 20%-80% more dust being present even at moderate optical depths if the streaming instability is active.

Key words: hydrodynamics – instabilities – protoplanetary discs – planets and satellites: formation

1 INTRODUCTION

In the process of planet formation, planetary embryos grow from the collisions of many millions of 1 km to 100 km sized planetesimals. In turn, planetesimals are born from millimetre-centimetre sized pebbles in protoplanetary discs. However, the formation of planetesimals cannot occur through simple pathways such as the collisional coagulation of progressively larger objects. It is well understood that collisions between objects in the range of 1 cm to 1 m in protoplanetary disc environments are predominantly destructive, resulting in smaller remnants from the original bodies in the collision (Zsom et al. 2010; Güttler et al. 2010; Windmark et al. 2012). Further, all solid objects orbiting in protoplanetary discs experience a headwind as they orbit through the gaseous component of the disc. At ~1 m sizes, this process is maximally efficient, and causes the rapid orbital decay of these objects, sending them into the central star on timescales on the order of a few hundred years (Weidenschilling 1977b).

Hence, planet formation requires a mechanism that is capable of rapidly forming planetesimals directly from cm sized pebbles. A leading candidate for this process is known as the streaming instability (SI), first studied by Youdin & Goodman (2005) (see also: Youdin & Johansen 2007; Johansen & Youdin 2007). The SI is a specific example of a broader family of resonant drag instabilities that exist when the aerodynamic drag timescale becomes resonant with another dynamical timescale in the disc (Squire & Hopkins 2018, 2020). In the saturated, non-linear phase of the instability,

the SI is capable of producing strong, localized overdensities of clouds of pebble-sized dust that can then gravitationally collapse into planetesimals (Johansen et al. 2007), thus directly overcoming the aforementioned growth barriers.

Since the seminal work from Johansen et al. (2007), over a decade of research has explored planetesimal formation via the SI with high resolution 3D hydrodynamic simulations (Johansen et al. 2009, 2012, 2015; Simon et al. 2016, 2017; Schäfer et al. 2017; Abod et al. 2019; Li et al. 2019; Nesvorný et al. 2019, 2021; Gole et al. 2020; Rucska & Wadsley 2021; Carrera et al. 2021, 2022; Carrera & Simon 2022). The streaming instability has proven to be a robust mechanism for forming planetesimals, so long as the local protoplanetary disc region meets the prerequisite conditions of enhanced dust mass concentration (i.e. supersolar) and sufficiently large dust grains (Carrera et al. 2015; Yang et al. 2017; Li & Youdin 2021). Protoplanetary discs observed with the Atacama Large Millimeter/submillimeter Array (ALMA) and the Very Large Telescope (VLT)/SPHERE and Subaru/HiCIAO have shown features with concentrated dust mass, such as rings (e.g. Dullemond et al. 2018; Macías et al. 2019; Muto et al. 2012; Avenhaus et al. 2018), non-axisymmetric bumps (e.g. van der Marel et al. 2013, 2015; Cazzoletti et al. 2018; van der Marel et al. 2021) and spiral structure (e.g. Benisty et al. 2015; Pérez et al. 2016; Benisty et al. 2017). Some rings may have sufficiently high dust concentrations to initiate planetesimal formation via the SI (Stammler et al. 2019; Maucó et al. 2021). Indeed, Carrera et al. (2021), Carrera et al. (2022) and Xu & Bai (2022a,b) show that persistent radial gas pressure maxima, which likely play a role in the formation

★ E-mail: wadsley@mcmaster.ca

of the observed large-scale rings (Whipple 1972), can sufficiently concentrate dust to trigger planetesimal formation via the SI.

Observations of minor solar system bodies support the idea that these objects may have been formed via the SI or a similar process. Asteroids are commonly described as “rubble piles”: gravitationally bound conglomerates of smaller pebbles with significant bulk porosity (Walsh 2018). Further, results from the Rosetta mission to comet 67P/Churyumov-Gerasimenko suggest this object likely formed from a cloud of millimetre-sized dust particles (Blum et al. 2017; Fulle & Blum 2017). Results from the New Horizons flyby of the Kuiper belt object (486958) Arrokoth suggest that this object, a contact binary with two distinct lobes, is likely a result of the slow decay of a binary orbit, where the two progenitor objects formed via the gravitational collapse of a pebble cloud (McKinnon et al. 2020; Grishin et al. 2020; Marohnic et al. 2021). Nesvorný et al. (2019) and Nesvorný et al. (2021) also show that the gravitational collapse of dense pebble clouds from SI simulations can produce planetesimal binaries with properties similar to binaries observed in the Kuiper belt. Kavelaars et al. (2021) measured the size distribution of objects in the cold classical Kuiper belt and find it is well described by an exponential cut-off at large sizes—a feature predicted by the streaming instability.

The New Horizons mission also observed the craters that cover the 4 billion-year-old surfaces of the Pluto-Charon system, enabling an analysis of the inferred size distribution of the impactors from the early Solar system that produced those craters (Singer et al. 2019; Robbins & Singer 2021; Robbins et al. 2017). Singer et al. (2019) find a deficit of craters at small sizes, for impactors below $\lesssim 1\text{--}2$ km in diameter. Unfortunately, current limits on computational power prevent 3D simulations of the SI from providing any insights on the SI-formed planetesimal size distribution at these small sizes (Simon et al. 2016; Li et al. 2019; see Section 4.1 of Rucska & Wadsley 2021 for further discussion).

Observational constraints on planetesimal formation are difficult to acquire, yet there is a general agreement between observational data and predictions from models of planetesimal formation via the SI. To date, the SI remains a leading candidate for the efficient formation of planetesimals, yet there remains open questions regarding this process, such as how the presence of a distribution of dust grain sizes affects outcomes regarding planetesimal formation.

1.1 Dust grain size distributions in protoplanetary discs

Observations reveal that protoplanetary discs in nature have at least two distinct dust populations (e.g. Franceschi et al. 2023): \sim millimetre-sized pebbles which have settled to the disc mid-plane and are most readily visible via their sub-mm wavelength thermal emission with ALMA (e.g. Andrews et al. 2016; van der Marel et al. 2021; Maucó et al. 2021), and \sim micron-sized grains suspended vertically in the disc, seen in infrared scattered light (e.g. Muto et al. 2012; Benisty et al. 2015; Avenhaus et al. 2018). Though these components occur in spatially distinct regions in the disc, they are likely linked, as grain growth theory shows that pebbles can readily grow via coagulation from the micron-size grains that the disc inherits from the interstellar medium (Birnstiel et al. 2011, 2015, see Birnstiel et al. 2016, for a review). Once the grain growth/fragmentation process reaches equilibrium, the predicted outcome from the widely-used Birnstiel et al. (2011) model is a grain size distribution described by multiple power-laws and a distinct peak, so that most of the mass in the distribution is within a factor of two of a specific grain size.

1.2 Streaming instability with a distribution of grain sizes

Until recently, there were few studies of the streaming instability with multiple sizes. Johansen et al. (2007) included multiple dust species in a subset of their runs, but the focus of their work was the onset of planetesimal formation rather than the behavior of the different grains. Bai & Stone (2010b) modelled discs with a variety of grain size distributions simultaneously in 3D simulations, and explored the influence of these distributions on properties of the non-linear, saturated state of the SI, pre-planetesimal formation.

Recently, there have been multiple studies on how particle size distributions influence the linear growth phase of the SI (Krapp et al. 2019; Paardekooper et al. 2020, 2021; McNally et al. 2021; Zhu & Yang 2021) and the linear and non-linear phase in 2D numerical simulations (Schaffer et al. 2018, 2021; Yang & Zhu 2021). These studies explored linear SI growth rates and the clumping of dust in the non-linear phase for distributions with a wide range of grain sizes. Overall, they conclude that the SI can produce strong dust clumping so long as the local dust-to-gas mass density ratio is large, approaching unity, and that the grain size distribution involves sufficiently large grains (near approximately a centimetre in size). In this paper, we study dust that is well within the strong growth regime, and follow the non-linear phase of the SI all the way to planetesimal formation.

We expand upon prior work by Bai & Stone (2010b) (3D), Schaffer et al. (2018, 2021) (2D) and Yang & Zhu (2021) (2D). The grain size distributions in these studies are power laws, with exponents similar to the fiducial slope for interstellar grains from Mathis et al. (1977). In this study, we sample the grain size distribution of Birnstiel et al. (2011), which is the equilibrium outcome of a grain growth/fragmentation model applicable to the midplane of protoplanetary discs, where planetesimal formation is believed to occur. The Birnstiel et al. (2011) distribution deviates from a single power law and includes a peak at large sizes. Thus, in our discretized version of that grain size distribution, the spacing between the representative grain size for each bin is not equal, in linear or logarithmic space, which is unique from prior work on this subject.

We present the first 3D, vertically stratified simulations of the SI with multiple species of dust grains since Bai & Stone (2010b), and compare the non-linear development of the SI in dust with multiple sizes against data from our prior work which used a single size (Rucska & Wadsley 2021). We highlight the differences in the dust surface density distribution between multi-size and single-size models, along with a novel analysis that reveals the observational consequences of the strong dust clumping seen in our runs, and explore how grains of different sizes participate in planetesimal formation.

Our paper is organized as follows. In Section 2 we present our methods and choice of parameters and a discussion about the dust grain size distribution we model. Section 3 focuses on the different dust surface density distributions between our multi-size model and prior work with single grain sizes, and the observational consequences of these differences. Section 4 focuses on how the different grain sizes participate in the non-linear filament and planetesimal formation process. In Section 5 we summarize our key results and discuss how this paper influences the current understanding of planetesimal formation via the SI.

2 METHODS

We model a local portion of a near-Keplerian protoplanetary disc. We study the dynamics of a gas phase aerodynamically coupled to a

dust/solids phase. The specifics of our numerical and hydrodynamic set-up are nearly identical to those described in [Rucska & Wadsley \(2021\)](#), so we briefly summarize those methods here and refer a reader interested in a more detailed discussion to that paper.

We use the shearing sheet approximation of [Goldreich & Lynden-Bell \(1965\)](#) to track the local dynamics of a Cartesian frame co-rotating at the Keplerian orbital velocity. We employ the ATHENA hydrodynamics code ([Stone et al. 2008](#); [Stone & Gardiner 2009](#)) with the solids particle module ([Bai & Stone 2010a](#)) to numerically evolve the protoplanetary disc system. Vertically, the box is centred on the disc midplane ($z = 0$), and the co-rotating frame of reference leads to an imposed background velocity in the azimuthal (y) direction described by $(q\Omega x)\hat{y}$. Here x is the radial co-ordinate in the co-rotating frame, with $x = 0$ being the radial centre of the box, and q is the power-law index of the angular velocity with radial position in the disc, $\Omega \propto r^{-q}$, so that in Keplerian discs $q = 3/2$.

The equations that describe the dynamics of the gas and solids (dust) are

$$\frac{\partial \rho_g}{\partial t} + \nabla \cdot (\rho_g \mathbf{u}) = 0, \quad (1)$$

$$\frac{\partial \rho_g \mathbf{u}}{\partial t} + \nabla \cdot (\rho_g \mathbf{u} \mathbf{u}) = -\nabla P_g + \rho_g \left[-2\Omega \times \mathbf{u} + 2q\Omega^2 x \hat{x} - \Omega^2 z \hat{z} + \mu \frac{\bar{\mathbf{v}} - \mathbf{u}}{t_{\text{stop}}} \right], \quad (2)$$

$$\frac{d\mathbf{v}'_i}{dt} = 2(v'_{iy} - \eta v_K)\Omega \hat{x} - (2-q)v'_{ix}\Omega \hat{y} - \Omega^2 z \hat{z} - \frac{\mathbf{v}'_i - \mathbf{u}'}{t_{\text{stop}}} + \mathbf{F}_g, \quad (3)$$

where ρ_g is the gas mass density, P_g is the gas pressure, \mathbf{u} , is the velocity of the gas, \mathbf{v}'_i is the velocity of an individual dust particle in the frame of the background shear flow, and $\bar{\mathbf{v}}$ is the mass-weighted average velocity of the dust in a gas cell. The gas equation of state is isothermal, $P_g = \rho_g c_s^2$, where c_s is the sound speed. The quantity $\mu \equiv \rho_d/\rho_g$ is the local ratio of dust to gas mass density, and η controls the strength of the radially inward drag force on the dust, which is related to the steepness of the radial gas pressure gradient (see Section 2.1). The quantity t_{stop} is the time-scale for the exchange of momentum between the dust and gas phase, which depends on a local gas quantities such as density and temperature, and, crucially, the physical size of the dust grains. We discuss this parameter in more detail in Section 2.2 as it is central to the context for this paper.

For the numerical algorithms, as in [Rucska & Wadsley \(2021\)](#) we use the standard ATHENA options for the Reimann solver (HLLC), hydrodynamics integrator (corner transport upwind) and a semi-implicit integrator for the dust momentum equations with a triangular-shaped cloud scheme to interpolate the dust particle properties with the simulation grid. In equation 3, the background shear flow has been subtracted from the dust and gas velocities. Separating the advection of the shear velocity from local deviations leads to a more efficient and accurate numerical integration ([Masset 2000](#); [Johnson et al. 2008](#)). We use the shearing box boundary conditions, which are periodic in the azimuthal (y) and the vertical directions (z) and shear periodic in the radial (x) direction ([Hawley et al. 1995](#); [Stone & Gardiner 2010](#)).

The term \mathbf{F}_g in equation 3 represents the gravitational acceleration. Not all prior work on high-resolution studies of the non-linear SI includes the effects of the dust density field self-gravity, but since our study is in part focused on the properties of planetesimals, it is included here. Self-gravity enables the collapse of dense dust material into gravitationally bound objects (i.e. planetesimals). Following [Simon et al. \(2016\)](#), based on an implementation described

Table 1. Simulation parameters.

Run names	τ_s - grain stopping time(s)
S0, S1, S2, S3 (S)	0.314
M6-0, M6-1, M6-2, M6-3, M6-4 (M6)	0.036, 0.191, 0.270, 0.314, 0.353, 0.412
M12	0.021, 0.113, 0.170, 0.218, 0.256, 0.284, 0.305, 0.324, 0.342, 0.363, 0.390, 0.437
M18	18 values between 0.016 and 0.450
Domain Size ($L_x \times L_y \times L_z$)/ H_g 0.2 × 0.2 × 0.2	Grid Resolution $N_{\text{cell}} = N_x \times N_y \times N_z$ 120 × 120 × 120
$N_{\text{par}}/(N_{\text{species}} \times N_{\text{cell}})$ 1	Z 0.02 \tilde{G} 0.05 Π 0.05

and tested in [Rucska & Wadsley \(2021\)](#), this acceleration is computed via the gradient in the gravitational potential from the dust density field, and this potential is computed from the solution to Poisson's equation,

$$\mathbf{F}_g = -\nabla \Phi_d, \quad (4)$$

$$\nabla^2 \Phi_d = 4\pi G \rho_d. \quad (5)$$

Here G is the gravitational constant. Our parameterization of this constant is discussed further in the next section (equation 9). Note, we neglect the gravitational influence of the gas, since the density perturbations in the gas in these kinds of local protoplanetary disc models are very small ([Li et al. 2018](#)). We use the fast Fourier transform Poisson solver available in ATHENA ([Kim & Ostriker 2017](#)) to solve equation 5, shear periodic horizontal boundary conditions and vacuum boundary conditions vertically.

2.1 Physical and numerical parameters, initial conditions

In this section we discuss the physical parameters that influence the dynamics of our local protoplanetary disc system. In this study we choose identical or very similar values to previous work on these systems ([Simon et al. 2016](#); [Schäfer et al. 2017](#); [Johansen et al. 2012](#); [Li et al. 2018](#); [Gole et al. 2020](#); [Rucska & Wadsley 2021](#)). These parameters and our choices are summarized in Table 1 and briefly discussed in this section, with a more in-depth discussion of the stopping time parameter τ_s in Section 2.2.

The total mass of the dust particles is controlled by the ratio of dust mass surface density to the gas surface density

$$Z = \frac{\Sigma_d}{\Sigma_g}, \quad (6)$$

and we choose $Z = 0.02$, which is a slightly supersolar metal mass ratio. Note that our simulation domains model only a fraction of the vertical gas scale height while capturing the full dust scale height. Thus the effective surface density mass ratio within the simulation domain is higher than 0.02. Following the discussion from Section 2.4 of [Rucska & Wadsley \(2021\)](#), the ratio of total dust mass to total gas mass within the full simulation domain is approximately 0.25.

The radial gas pressure gradient represented by the $-2\eta v_K \Omega$

term in equation 3 is parameterized via η :

$$\eta = n \frac{c_s^2}{v_K^2}. \quad (7)$$

where n is the pressure power law index, $P_g \propto r^{-n}$, the local Keplerian speed is v_K , and the isothermal sound speed is c_s . This pressure gradient shifts the azimuthal component of the dust and gas velocities by ηv_K , and we subtract this shift from our data to conduct analysis in this shifted frame. As with other work, in our simulations η is ultimately controlled by a similar parameter

$$\Pi = \frac{\eta v_K}{c_s}, \quad (8)$$

and we choose $\Pi = 0.05$, a typical value that applies to a wide variety of disc models (Bai & Stone 2010b).

The strength of self-gravity versus tidal shear is controlled by

$$\tilde{G} \equiv \frac{4\pi G \rho_{g,0}}{\Omega^2}. \quad (9)$$

Selecting $\tilde{G} = 0.05$ is equivalent to a Toomre (1964) Q of 32, so the gas phase is gravitationally stable, supporting our exclusion of the gas density field in solving for the gravitational potential (equation 5).

In equation 9, $\rho_{g,0}$ is the gas midplane density. The gas density is initialized to have a Gaussian profile vertically with a scale height H_g , and a uniform distribution in the radial and azimuthal directions. The dust phase is initialized analogously except with a scale height of $H_d = 0.02 H_g$. We set the units of our scale-free model to that $\rho_{g,0} = H_g = \Omega = c_s = 1$. See Section 2.4 of Rucska & Wadsley (2021) for a discussion on how to convert these units to physical units. Using the minimum mass solar nebula model of Hayashi (1981) and placing our model at 3 AU, there is approx $1.5 M_{\text{Ceres}}$ worth of dust mass in our full simulation domain.

The 3D simulation domains we study have equal lengths of $L_x = L_y = L_z = 0.2 H_g$, and we choose a grid resolution of $N_x = N_y = N_z = 120$. Simon et al. (2016) show that this resolution and Rucska & Wadsley (2021) show that this box size is sufficient to accurately capture the planetesimal formation process with our chosen set of physical parameters. This grid resolution matches that of Rucska & Wadsley (2021).

We choose a dust resolution such that the total number of particles for each grain species is equal to the total number of grid points in the gas grid. The millions of dust particles are initially placed so that the overall dust density distribution is uniform in the x - y plane and follows a Gaussian profile vertically. The precise initial positions of the particles are set via a random number generator. As in Rucska & Wadsley (2021), we re-run multiple simulations that are otherwise identical except for the initial seed for the random number generator, which gives a different initial (and very small in amplitude) noise pattern to the dust density in each run. Once the streaming instability develops into the non-linear phase, the initial perturbations result in dramatic variations in the dust density. Thus, re-running simulations with different initial seeds probes the stochastic qualities of the non-linear SI and the variance in the outcomes in a way that a single simulation cannot.

In Table 1, the simulation labels S0, . . . , S3 denote the simulations which use a single dust grain size (these are the same L02(a-d) simulations from Rucska & Wadsley 2021), and analogously the labels M6-0, . . . , M6-4 represent five simulations that use multiple grain species simultaneously, with the only difference being the random seed that sets in the initial particle distribution. The M12 and M18 are simulations that sample the same size distribution as the M6-0, . . . , M6-4 simulations but with a greater number

of grain species/bins. Details on the grain sizes in each simulation are discussed in the proceeding section.

2.2 Grain size distribution

We base our distribution of grain sizes on the results from Birnstiel et al. (2011), a widely used model of the collisional growth and fragmentation of dust grains in protoplanetary discs. Dynamics such as local turbulence, vertical settling, and radial drift affect the relative velocities between dust grains and can lead to grain growth or fragmentation via destructive collisions, depending on local conditions (for a review, see Birnstiel et al. 2016).

Birnstiel et al. (2011) conclude that the dust grain population will equilibrate towards a size distribution with a shape that depends on properties of the disc (see their Fig. 6). Relevant properties include the gas surface density, midplane temperature, the Shakura & Sunyaev (1973) α turbulent viscosity parameter, and a fragmentation threshold velocity for the grains. The authors also provide an online tool for exploring different combinations of disc quantities. For the distribution shape we study, we choose $\Sigma_g = 100 \text{ g/cm}^2$, $T_{\text{mid}} = 100 \text{ K}$, roughly equivalent to a radial position of $\sim 5 \text{ AU}$ for a disc with $\Sigma_g(r) = 1000 (r/\text{AU})^{-3/2} \text{ g/cm}^2$ (e.g. minimum mass solar nebula model; Weidenschilling 1977a) and $T_{\text{mid}} = 200 (r/\text{AU})^{-3/7} \text{ K}$ (e.g. Chiang & Goldreich 1997). For other parameters we choose $\alpha = 1 \times 10^{-4}$, $v_{\text{frag}} = 3 \text{ m/s}$. These choices lead to a distribution that peaks around $\sim 4 \text{ cm}$.

The simulation impact of grain size is to set the characteristic time scale for the aerodynamic coupling between the dust and gas, t_{stop} (equations 2 and 3). There are different forms for this stopping time depending on the regime of drag one considers, but for protoplanetary discs, almost all grains are in the Epstein (Epstein 1924) drag regime (Birnstiel et al. 2016), where the size of the dust grains is smaller than the mean free path of the gas particles. The form of t_{stop} in this regime is

$$t_{\text{stop}} = \frac{\rho_s}{\rho_g c_s} s, \quad (10)$$

where ρ_s is the material density of the particles (approximately 2.6 g cm^{-3} for silicates; Moore & Rose 1973), ρ_g is the local gas density, c_s is the local sound speed, which depends on the gas temperature, and s is the size of the dust grains. Thus, for the same gas properties, t_{stop} scales linearly with grain size. In our models, as with other studies of the streaming instability, we model the drag coupling between the dust and gas with a dimensionless parameter $\tau_s = t_{\text{stop}} \Omega$,

$$\tau_s = \frac{\Omega \rho_s s}{\rho_g c_s}. \quad (11)$$

In our disc model, the midplane gas density is $\rho_{g,0} = (1/\sqrt{2\pi})(\Sigma_g/H_g)$ and $H_g = c_s/\Omega$ (Armitage 2020), so that $\tau_s = (\rho_s/\Sigma_g)s$. With our above choices for the disc properties in the grain size distribution, the previous mentioned size peak of 4 cm grains translates to $\tau_s \sim 0.1$. In this study, we wish to directly compare our results to both our previous study (Rucska & Wadsley 2021) and prior work which has focused on a single stopping time of $\tau_s = 0.314$. Thus, we maintain the original shape of this particular Birnstiel et al. (2011) distribution from our chosen disc parameters, but slightly shift the peak to $\tau_s = 0.314$. Within the model of Birnstiel et al. (2011) this is equivalent to moving the fragmentation threshold from 3 km/s to $\sim 5 \text{ km/s}$ or modifying the temperature profile. Setting the peak at our previous single grain size value al-

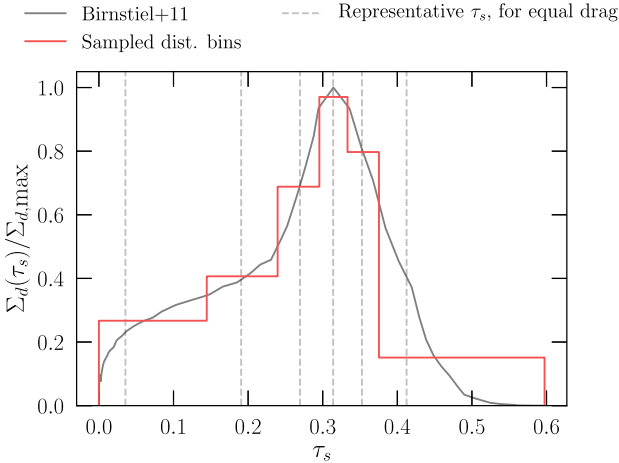


Figure 1. Grain size distribution sampled for this study. The grey curve represents the surface density distribution as a function of grain size according to a grain growth model in collision-fragmentation equilibrium (Birnstiel et al. 2011). The red curve represents our sampling of the distribution with six bins, and the vertical dashed lines are the representative τ_s selected for each bin (See Section 2.2.1).

allows us to directly compare these two different representations of the dust environment.

2.2.1 Sampling the Birnstiel et al. (2011) distribution

Figure 1 shows the dust mass surface density distribution that we sample, as a function of τ_s . The six different bins (red curve), used for the five M6-0...M6-4 simulations, are chosen such that there is roughly equal dust mass in each bin while enforcing that one bin is centred on the peak at $\tau_s = 0.314$. Since the streaming instability is driven by the aerodynamic coupling between the dust and gas, we chose the representative τ_s for each bin so that there is the same total drag force (proportional to Σ_d/τ_s) in each bin as in the original distribution. This requires us to satisfy the equality

$$\int_{\tau_{\text{bin},l}}^{\tau_{\text{bin},r}} \frac{\Sigma_d(\tau_s)}{\tau_s'} d\tau_s' = \frac{\Sigma_{\text{bin}}}{\tau_{\text{bin}}} (\tau_{\text{bin},r} - \tau_{\text{bin},l}), \quad (12)$$

where $\tau_{\text{bin},(r,l)}$ are the right and left τ_s values in each bin, Σ_{bin} is the mean height of the distribution in that bin, and τ_{bin} is the representative size in that bin which we solve for. We see from Figure 1 that τ_{bin} in the bins for $\tau_s > 0.1$ roughly tracks the half-mass point of the $\Sigma_d(\tau_s)$ curve, but in the bin for the smallest grains, τ_{bin} is closer to the leftmost, small- τ_s edge of the bin, because the drag force per unit mass scales as $1/\tau_s$.

Table 1 lists the exact values of τ_{bin} (hereafter just referred to by τ_s) modelled simultaneously by our simulations, with each species given a roughly equal amount of the total dust mass in the simulation domain¹. Note that these values of τ_s are not equally spaced, linearly or logarithmically, which is different from the distributions modelled by prior work (Johansen et al. 2007; Bai & Stone 2010b; Schaffer et al. 2018; Yang & Zhu 2021) which also used equal-mass bins in their discretized distributions.

¹ We could not simultaneously ensure that our sample has one bin with a representative τ_{bin} exactly at the peak $\tau_s = 0.314$ and have the bins contain exactly equal mass. However all bin total masses are within 10% of each other.

2.2.2 Increasing the number of grain species

To accompany our main M6-0...M6-4 simulations which use 6 bins, we also run two simulations with more species of grains/bins in order to test how our results are affected by the number of species present. We ran one with 12 bins and the other with 18 bins, which we denote M12 and M18 respectively. When creating these samples with additional bins, we decide to subdivide each of the original 6 bins into 2 and 3 bins, again keeping an equal mass in each bin. This maintains the original bin edges from the 6-bin sample and thus allows for a more straightforward comparison of the results between the different discrete distributions. Once the new (additional) bin edges are computed, the same procedure of equal drag from equation 12 is used to select a representative τ_s for each bin.

2.3 Planetesimal/clump identification

To quantify how the different sized grains participate in the formation of planetesimals in our simulations, we must first identify which grains are a part of bound planetesimals. For this study, we accomplish this with a dust density cut. The Hill radius denotes a region where the gravity of an object in a circumstellar disc dominates over the shear due to the velocity gradient of the background Keplerian rotation. This shear is the only force that directly opposes the gravitational collapse of the dust. As described in Rucsa & Wadsley (2021), we can convert the Hill radius into a Hill density, above which a dust clump is unstable to gravitational collapse. In the physical parameters of our model, this Hill density is given by,

$$\rho_H = 9 \frac{\Omega^2}{4\pi G}. \quad (13)$$

With our choices of parameters, $\rho_H = 180$.

We identify all particles within cells with dust densities greater than ρ_H as being a part of bound planetesimals, and all adjacent cells above this threshold are considered the same planetesimal. The triangular shaped cloud scheme that translates particle data to the gas grid smooths the dust density on the length scale of a single grid cell. As a result, some cells with relatively few particles have a dust density above ρ_H because there are tens of thousands of particles in the neighbouring cells. We also average clump-related data over the multiple M6-0...M6-4 simulations, removing some of the influence of the stochastic nature of the non-linear SI from our results concerning planetesimals. In this paper, we are not interested in the details of the clump mass distributions so we do not opt for a more sophisticated clump finding algorithm as in Rucsa & Wadsley (2021).

3 DUST SURFACE DENSITY AT DIFFERENT GRAIN SIZES

In this section we examine the dust surface density in the multiple-grain simulations (M6-0, ..., M6-4, hereafter referred to collectively as M6) and compare them with the surface density from the single-grain simulations (S0, ..., S3, hereafter S). We inspect the surface density maps visually and then present a quantitative analysis of rudimentary observational consequences resulting in differences from these maps.

The dust surface density in the 6 different sizes or species of dust grains at $t = 100\Omega^{-1}$ in the M6-0 simulation is shown in Figure 2. We present all data from single snapshots at $t = 100\Omega^{-1}$ because at this stage planetesimal formation has begun in earnest, but the planetesimals have not yet disrupted the other features in the

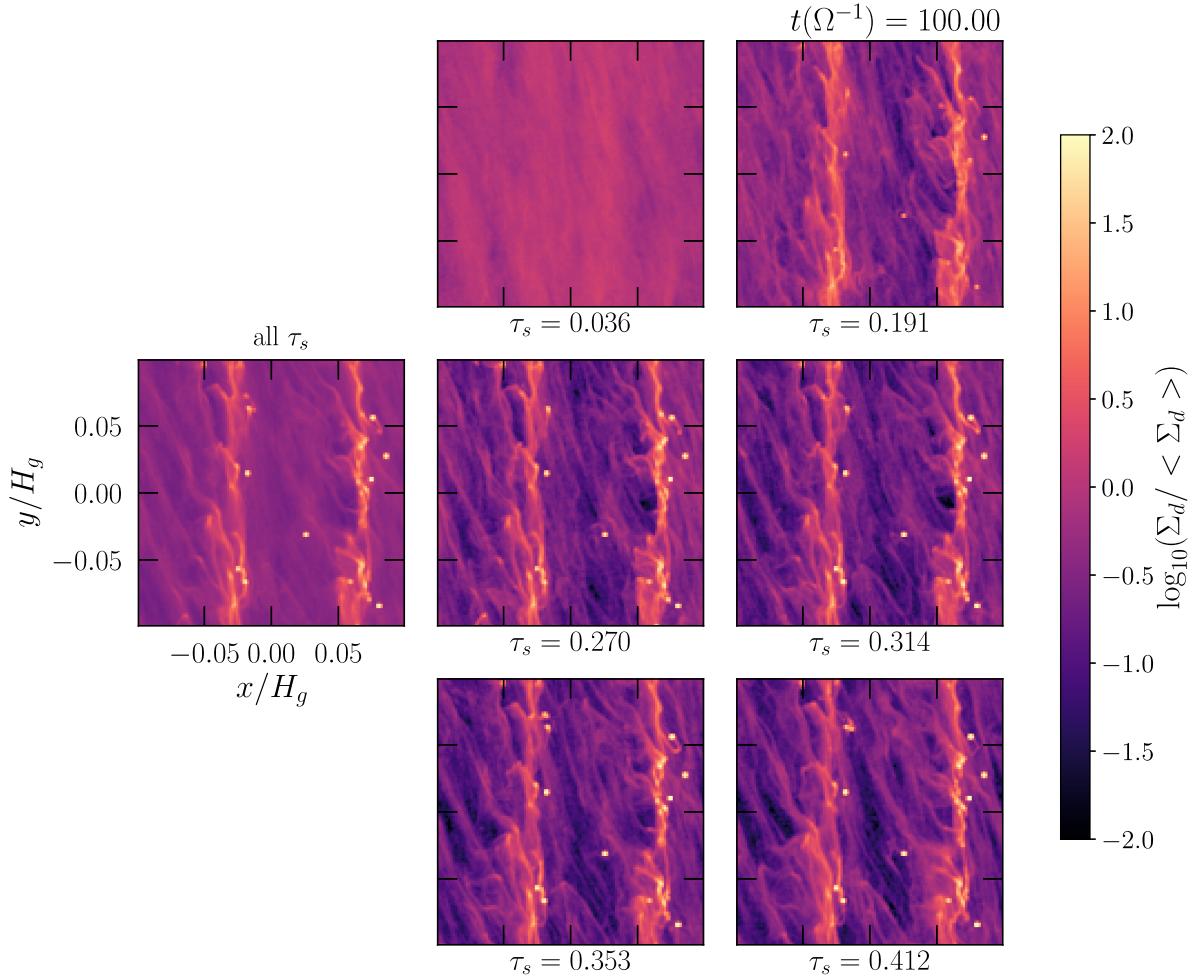


Figure 2. Dust surface density in the x - y (radial-azimuthal) plane for each species of grain in the M6-0 simulation. The two right columns represent the surface density in the individual species, each identified by their grain size which here is represented by the dimensionless stopping time, τ_s (see equation 11 and surrounding discussion). The lone panel in the left column represents the total dust surface density in the simulation, with all grain species. The colour represents the logarithm of the dust surface density normalized by the mean dust surface density. The mean and normalization is computed in each panel individually. These data represents the simulation at time $t = 100$ in units of the inverse orbital frequency, Ω^{-1} .

dust such as the filaments. As we discuss in detail in Section 4.1 of Rucska & Wadsley (2021), the numerical cross-sections of the planetesimals in our simulations (and all similar simulations in the literature) are unphysically large, which causes the planetesimals to post-formation interact more strongly with the other dust particles than we would expect in nature. Thus, the true final state of the dust surface density post planetesimal formation is uncertain. We pick $t = 100\Omega^{-1}$ as a compromise to capture the coexistence of the planetesimals and the filaments, which we expect to be typical of the saturated stage of the non-linear streaming instability.

We notice immediately in Figure 2 that the smallest sized dust grains (lowest τ_s) do not readily collect into filaments or planetesimals at all, even when the larger grains are producing dense features simultaneously. All grains with $\tau_s > 0.1$ participate in the structure of the filaments, while the distribution of the $\tau_s = 0.0355$ grains is smooth with relatively little spatial variation. Secondly, with a more careful visual inspection of the $\tau_s = 0.191$ surface density map, one can see that the brightest, ~ 2 -3 cell wide objects in the largest grains—which represent the planetesimals—are less bright than in the $\tau_s > 0.2$ grains, suggesting the $\tau_s = 0.191$ grains do not incor-

porate into planetesimals as readily (for more quantitative results concerning clumping, see Section 4). In the full dust surface density, which includes all grains (“all τ_s ” panel), we see altogether the filaments, planetesimals, and the smooth, dispersed quality of the smallest grains which is most apparent in the space between filaments. Similar visual features can be seen in other studies of the non-linear SI with multiple grain sizes (cf. Yang & Zhu 2021 Figures 4 and 6, Bai & Stone 2010b Figure 2, Johansen et al. 2007 Figure 2).

We can make similar observations when comparing the surface density maps of the M6 and S simulations, shown in Figure 3. The S cases use one grain size of $\tau_s = 0.314$ and thus more closely resemble the $\tau_s = 0.270$ to 0.412 grains from the M6 simulations, in that the dust mass at these sizes is predominantly concentrated into planetesimals and filaments which are separated by relatively empty regions with surface densities $\leq 10\%$ of the mean surface density. The smaller grains in the M6 simulations fill these empty regions.

More quantitative confirmation of these observations can be seen in the probability distribution functions (PDFs) of the dust surface density, in Figure 4. The top panel shows the PDFs for the

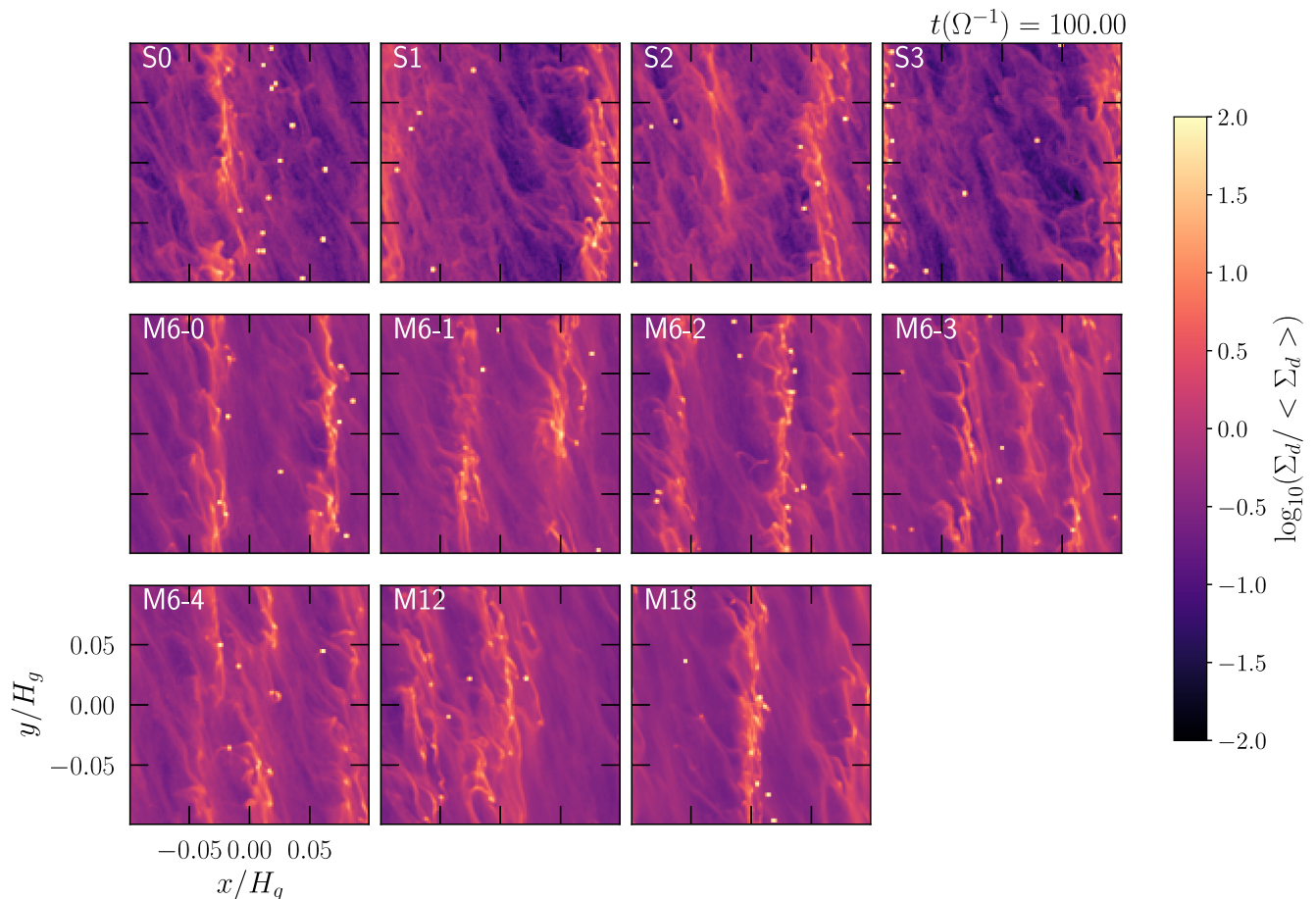


Figure 3. Dust surface density at $t = 100 \Omega^{-1}$ in the x - y (radial-azimuthal) plane for all simulations. The S simulations use a single grain size, and the $M6$ simulations use multiple sizes simultaneously. See Table 1 for a summary of the simulation parameters.

individual grains from the M6-0 simulation at $t = 100 \Omega^{-1}$. Here, we quantify what is observable in Figure 2: the distribution of surface density in the $\tau_s = 0.036$ grains is narrow, peaking around the mean, $\langle \Sigma_d \rangle$. The $\tau_s = 0.191$ distribution is wider by an order of magnitude in each direction, which is a sign that these grains are participating in filaments. Yet only the grains with $\tau_s > 0.2$ extend out to surface densities greater than $100 \langle \Sigma_d \rangle$ – a (rough) proxy for planetesimals. The PDFs of the particle volume density from Yang & Zhu (2021) Figure 8 show similar segregation by grain size.

The bottom panel of Figure 4 highlights how this affects the overall surface density in the M6 simulations. The PDFs extend only as low as $0.1 \langle \Sigma_d \rangle$, while the distributions from the single size $\tau_s = 0.314$ simulations extend out to $0.01 \langle \Sigma_d \rangle$. Interestingly, when looking at the $\tau_s = 0.314$ grains from the M6 simulations on their own, these PDFs show there are more low surface density areas in these grains than there are in the S simulations at this size. This suggests that the presence of different-sized dust grains in the M6 results in more empty or lower surface density regions than if the $\tau_s = 0.314$ grains were left to evolve on their own.

The PDFs for the M12 and M18 simulations—which have more grain size bins than the M6 simulations—are also shown in the bottom panel of Figure 4. These PDFs follow the M6 data closely, suggesting that six grain species was sufficient to capture the main effects on the dust surface density.

The differences in the S (blue) and $M6$ (red) PDFs have inter-

esting observational consequences. There are many more regions with low surface density in the S simulations and (on average) more regions at higher surface densities. Depending on the opacity of the dust, this could lead to a lower estimate of the total dust mass from observations due to optical depth effects. We explore this idea in the next section.

3.1 Observational consequences

Observations of some bright rings in protoplanetary discs have come to the interesting conclusion that the thermal emission from the dust in these rings is likely not optically thick (Dullemond et al. 2018; Huang et al. 2018; Cazzoletti et al. 2018; Macías et al. 2019; Maucó et al. 2021). Other studies have shown that, with a parameterized model of planetesimal formation via the streaming instability, this can be explained by pebble-sized dust in rings being converted into planetesimals, which do not contribute to mm wavelength emission (Stammler et al. 2019; Maucó et al. 2021). Taking this idea a step further, Scardoni et al. (2021) used the dust surface density profiles from 2D simulations of the SI and explored how the dust clumping would affect observations. They use a complex model for the dust opacity (Birnstiel et al. 2018) and find general agreement between their calculations of observed properties of discs such as the fraction of the emission that is optically thick and the spectral index. Unsur-

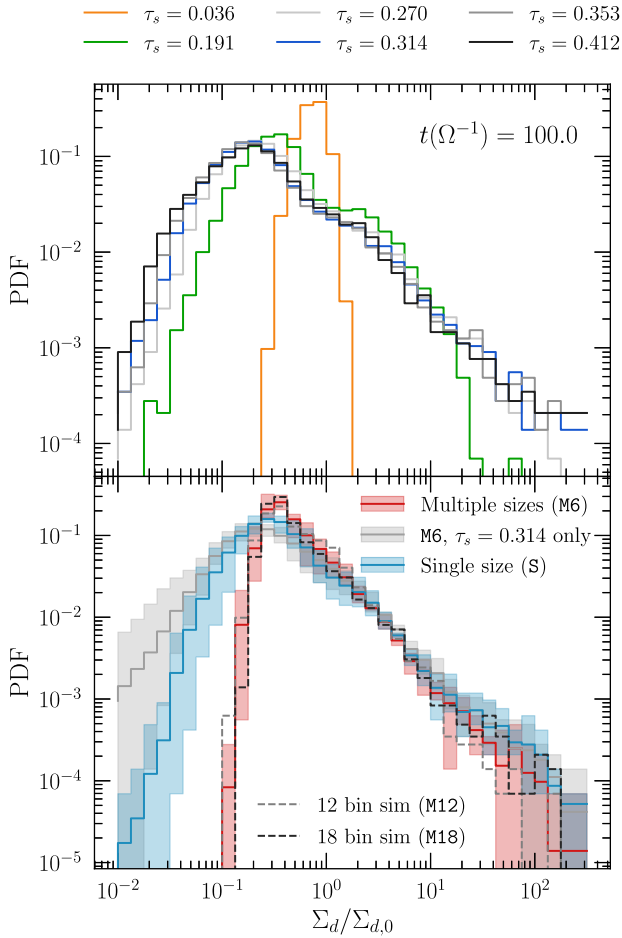


Figure 4. Probability distribution functions (PDFs) of the dust surface density in our simulations at $t = 100\Omega^{-1}$. *Top.* PDF for the M6-0 simulation for each τ_s (grain size) bin (cf. Figure 2). The normalization by the mean surface density is computed for each grain species individually. *Bottom.* PDFs for all simulations (cf. Figure 3). The red (blue) shaded regions represent the maximum and minimum bounds among all M6 (S) simulations, and solid line represents the mean PDFs. The grey shaded data and solid line represent the $\tau_s = 0.314$ grains from the M6 simulations only. The dashed curves are the PDFs for the M12 and M18 simulations.

prisingly, they conclude that planetesimal formation can reduce the optical depth of emission at mm wavelengths.

In this section, we construct two mass correction factors which quantify the observational implications of the varying degrees of dust clumping seen in our simulations². We explore how these mass correction factors vary with optical depth ($\tau_{\text{opt}} = \kappa\Sigma_d$), and how they evolve over time. Note that to leading order effects like disc inclination can be wrapped into a different effective κ . We forgo a detailed mock observational treatment and complicated calculations of the dust opacity. Instead, we examine how the mean emission is modified due to both unresolved structure from the SI and differences between single grain size and multiple grain size models.

The intensity of emission (I) from a source of radiation (source function S , and other dust physical properties assumed constant),

² Note, the dust features created by the SI occur on length scales several orders of magnitude below 1 AU, and are hence unresolvable by any contemporary observational facility.

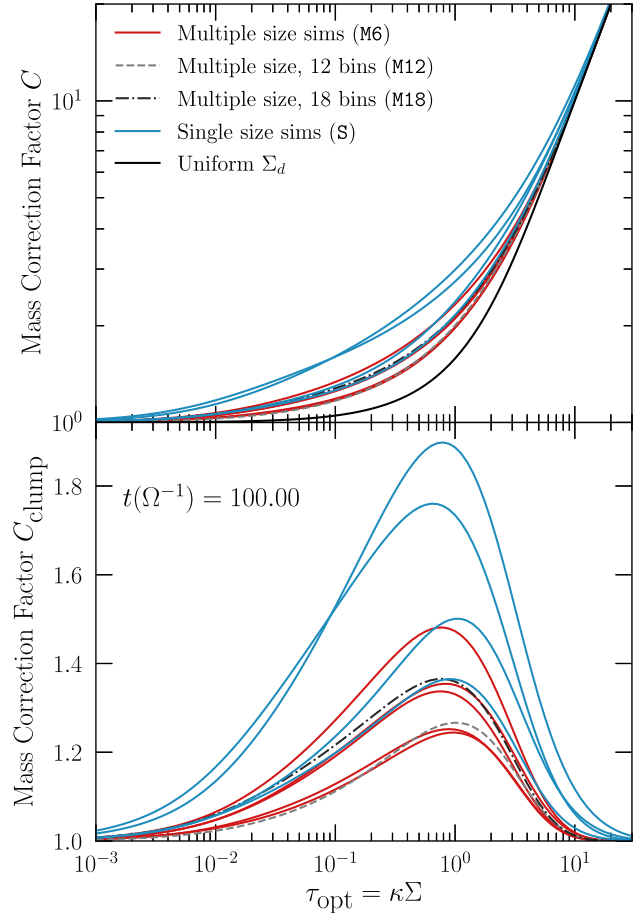


Figure 5. Observational dust mass correction factors. *Top.* C : The ratio of the true surface density (Σ_d) to an estimate that assumes the disc to be optically thin with no unresolved structures within the beam, as a function of the mean optical depth. *Bottom.* C_{clump} : The correction factor due to unresolved clumping from the streaming instability alone, with uniform optical depth effects removed. These curves are equivalent to dividing the coloured and dashed curves in the top panel by the solid black curve in the top panel. *Both.* Each blue or red curve represents an individual simulation. Details on how these factors are defined are in Section 3.1.

can be expressed as,

$$I(\tau_{\text{opt}}) = S(1 - e^{-\tau_{\text{opt}}}), \quad (14)$$

where τ_{opt} is the optical depth, and the wavelength dependence of all quantities has been ignored. We consider a simple prescription for the optical depth, $\tau_{\text{opt}} = \kappa\Sigma$, where κ is the dust opacity and Σ is the dust surface density. For optically thin emission (low opacity, and/or low surface density), $\tau_{\text{opt}} \ll 1$, and then $I \approx S\kappa\Sigma$, linear in the surface density. If S and κ are known, we can estimate $\Sigma_{\text{est}} = I/S\kappa$. However, assuming the emission is optically thin systematically underestimates the surface density at points where τ_{opt} is not small, as,

$$\Sigma_{\text{est}} = \frac{(1 - e^{-\kappa\Sigma})}{\kappa}. \quad (15)$$

This expression is useful as it does not require knowledge of the source function to assess the potential for systematic errors.

We take the surface density map from our simulations, $\Sigma_d(x, y)$, and compute an converted surface density map, $\Sigma_{\text{est}}(x, y)$, via equation 15. We allow for a wide range of constant opacities,

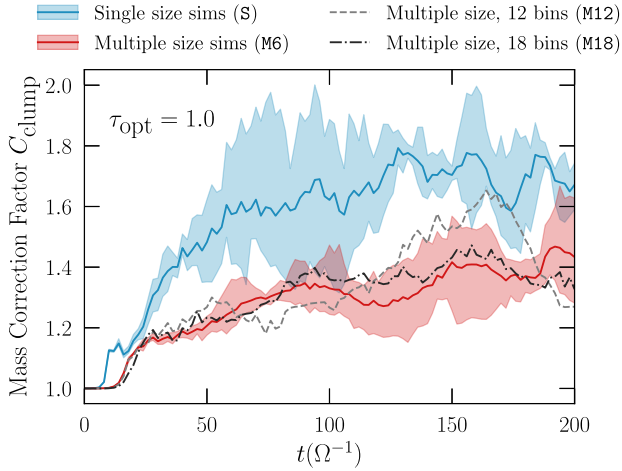


Figure 6. The dust mass correction factor C_{clump} over time in all simulations, at an optical depth of $\tau_{\text{opt}} = 1.0$. The shaded regions are bounded by the maximum and minimum values across the sample of multiple simulations, and the solid curves represent the means of that sample.

κ , acknowledging that there are large uncertainties in the values of dust opacity (Birnstiel et al. 2018). We then take the spatial average, using the fact that all features in our simulations would be unresolved within an observational beam. Henceforth, we will refer to this average using, $\Sigma_{\text{est}} = \langle \Sigma_{\text{est}}(x, y) \rangle$.

Finally, we construct two dust mass correction factors from these average estimate surface densities. First, using a ratio of the true averaged dust surface density of the simulation Σ_{actual} (i.e. $\Sigma_{\text{actual}} = \langle \Sigma_d(x, y) \rangle$),

$$C = \frac{\Sigma_{\text{actual}}}{\Sigma_{\text{est}}}. \quad (16)$$

C is an overall correction factor for optically thick, unresolved clumping.

To examining clumping alone, we can compute a new estimate, $\Sigma_{\text{est, uniform}}$, assuming a *uniform* dust density distribution, $\Sigma(x, y) = \langle \Sigma(x, y) \rangle$, and compare that to Σ_{est} from our strongly clumped simulations. The ratio,

$$C_{\text{clump}} = \frac{\Sigma_{\text{est, uniform}}}{\Sigma_{\text{est}}} = \frac{C}{C_{\text{uniform}}}, \quad (17)$$

measures the correction associated with of dust clumping only (here due to the streaming instability). $C_{\text{uniform}} = \Sigma_{\text{actual}}/\Sigma_{\text{est, uniform}}$ is the correction associated assuming low optical depths. If one is confident about the optical depth of an observed source, C_{clump} represents the factor the inferred dust surface density should be multiplied by if the SI is believed to have caused significant unresolved clumping in that region of the disc.

The top panel of Figure 5 shows C as a function of τ_{opt} . At low τ_{opt} , $C \sim 1$ for all simulations, since in this regime the optically thin assumption is valid by definition. At intermediate τ_{opt} , expected variation between simulations (Rucsa & Wadsley 2021) leads to a spread in C . At high τ_{opt} , all simulations converge to $C \sim \tau_{\text{opt}}$ since the exponential term in equation 15 vanishes, removing any dependence in C on the surface density distribution in the simulations and hence any influence of clumping. It is at intermediate values of τ_{opt} where differences between the sets of simulations are apparent.

To understand the impact of clumping, we look at the clumping correction factor, C_{clump} , in the bottom panel of Figure 5. This

factor is the ratio of C for each simulation (coloured and dashed lines, top panel) to C_{uniform} , calculated for a spatially uniform dust surface density distribution at $\langle \Sigma_d \rangle$ (black line, top panel³). Hence, what C_{clump} highlights is the influence of the different amount of clumping in the dust surface density maps/distributions between the two sets of simulations (Figure 3 and 4). If the optical depth is well constrained (e.g. from grain properties), it is the factor one would multiply a dust surface density inferred from observations by in order to account for the (unresolved) dust clumping from our simulations.

We note that C_{clump} peaks near $\tau_{\text{opt}} = 1$ for all simulations, with peak values generally higher for the single size simulations S than the $M6$ simulations with multiple sizes. As we discussed earlier in Section 3, when compared the simulations with multiple grains, the dust in the S sims is more heavily concentrated into denser structures. As a consequence, in our simple model, the dust emission from the S models is overall less bright than the $M6$ models, as there is relatively less dust mass in the inter-filament space, and there is more dust in the filaments and planetesimals, where the emission is saturated at intermediate optical depths. Thus more of the dust mass is “hidden” in the S simulations.

The peak values of C_{clump} are between $\sim 1.2 - 1.5$ for the $M6$ and $M12$ and $M18$ simulations, which we believe to be more representative of protoplanetary disc grain size distributions in nature rather than a single size. Thus, for dust grains described by a Birnstiel et al. (2011) grain size distributions with stopping times peaked at $\tau_s = 0.314$, observational estimates of the dust mass from protoplanetary discs could be too low by a factor of 20 – 30% in regions of the disc where the streaming instability is active. If the grain size distribution were instead much more strongly peaked at a single size—i.e., closer to the S models than $M6$ —then the clumping mass correction factor could be as high as factor of two.

The values of C_{clump} for a mean optical depth, $\tau_{\text{opt}} = 1.0$, over time, plotted in Figure 6, are fairly stable over the course of our simulations. Once planetesimal formation begins, the main features of the dust surface density which influence C_{clump} persist over dozens of dynamical timescales. Note that the single snapshot values of C_{clump} presented in Figure 5 are from $t = 100 \Omega^{-1}$, and in Figure 6 this is one of the rare times where there is slight overlap between the single size and multiple size sims. At most other times the curves in Figure 5 do not overlap at all. Similar to the single snapshot data, the curves for the $M12$ (12 bins) and $M18$ (18 bins) simulations in Figure 6 are consistent with the $M6$ simulations, suggesting incorporating more grain species does not influence our results.

Note, we do not plot C over time as it has the same shape of C_{clump} , since the difference in normalization between C and C_{clump} (at a specific optical depth) are just different constant factors. C uses $\langle \Sigma_d \rangle$ as a reference point, and, for the purposes of Figure 6, C_{clump} uses $\langle \Sigma_{d, \text{unif}} \rangle(\tau_{\text{opt}} = 1.0)$.

4 PLANETESIMAL COMPOSITION: GRAIN SIZE

In this section we explore the composition of these clumps in terms of the various dust species within them, as well as the composition of the dust mass that lost from each clump from simulation snapshot to snapshot. The bright cells in the surface density maps in Figure 3 indicate that all simulations from our study produce dense,

³ This curve is simply a plot of $\tau_{\text{opt}}/(1 - \exp(-\tau_{\text{opt}}))$.

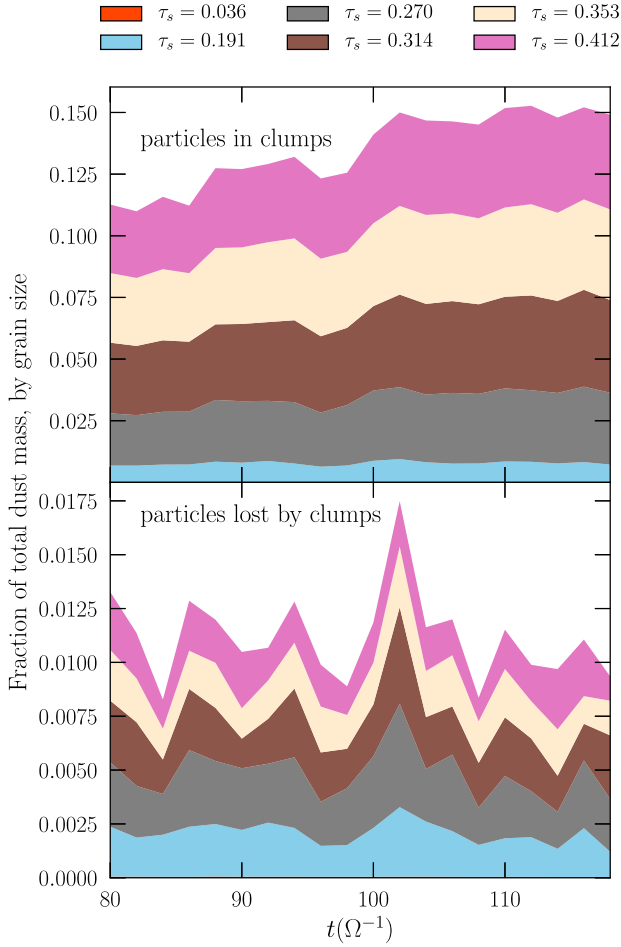


Figure 7. Fraction of total dust mass for particles in bound clumps or lost by clumps, for each τ_s (grain size) bin. These data represent an average over the whole group of M6 simulations. The coloured bands represent the fractional mass for each τ_s . The data for each grain size are vertically stacked so that the total mass in clumps (or lost by clumps) for all dust grains is tracked by the top of the pink shaded region. The data for $\tau_s = 0.036$ are too small to be seen on this scale; see Table 2 for time-averaged values of these data for all τ_s , and for the data from the M12 and M18 simulations.

gravitationally bound clumps. As described in Section 2.3, we identify bound clumps (i.e. planetesimals) as regions where the 3D dust volume density (ρ_d) exceeds the Hill density (ρ_H) threshold above which it is unstable to gravitational collapse.

The fraction of mass in clumps for each grain size is shown in Figure 7. The different coloured bands represent the mass in each grain size bin. Table 2 shows the time averages for these data over the range of time across the full x -axis in Figure 7. As seen in the top panel and in Table 2a, the majority of the mass in clumps ($> 90\%$) is in the grains with $\tau_s > 0.2$. A small fraction of the clumps are composed of $\tau_s = 0.191$ grains and there is effectively no clump mass associated with the $\tau_s = 0.035$ grains. These results corroborate earlier observations from Figure 2 regarding the decreased prominence or total lack of visible planetesimals in the surface density maps for these grain sizes.

Some particles that are within a clump in one snapshot are not within that same clump⁴ in the consecutive snapshot. These

Table 2. Time averages ($t = 80 - 120\Omega^{-1}$) of the total dust mass in bound clumps and lost by clumps, split by τ_s (grain size) (cf. Figure 7).

(a) Dust mass in bound clumps (as fraction of total dust mass).

τ_s	6 bin runs	12 bin	18 bin
0.036	4.90×10^{-5}	4.38×10^{-4}	5.84×10^{-4}
0.191	7.73×10^{-3}	7.47×10^{-3}	1.08×10^{-2}
0.270	2.60×10^{-2}	1.81×10^{-2}	3.20×10^{-2}
0.314	3.38×10^{-2}	2.29×10^{-2}	4.23×10^{-2}
0.353	3.30×10^{-2}	2.24×10^{-2}	4.33×10^{-2}
0.412	3.43×10^{-2}	2.06×10^{-2}	4.46×10^{-2}

(b) Dust mass lost by clumps (as fraction of total dust mass).

τ_s	6 bin runs	12 bin	18 bin
0.036	4.71×10^{-5}	2.74×10^{-4}	3.52×10^{-4}
0.191	2.04×10^{-3}	1.99×10^{-3}	2.70×10^{-3}
0.270	2.78×10^{-3}	2.51×10^{-3}	3.83×10^{-3}
0.314	2.43×10^{-3}	2.21×10^{-3}	3.38×10^{-3}
0.353	1.95×10^{-3}	1.75×10^{-3}	2.73×10^{-3}
0.412	1.93×10^{-3}	1.72×10^{-3}	2.55×10^{-3}

Table 3. Residence time (equation 18) for the different dust grains in the M6 simulations.

τ_s	Mass in clumps	Mass lost from clumps	Residence time (Ω^{-1})
0.036	4.90×10^{-5}	4.71×10^{-5}	2.08
0.191	7.73×10^{-3}	2.04×10^{-3}	7.60
0.270	2.60×10^{-2}	2.78×10^{-3}	18.7
0.314	3.38×10^{-2}	2.43×10^{-3}	27.8
0.353	3.30×10^{-2}	1.95×10^{-3}	33.9
0.412	3.43×10^{-2}	1.93×10^{-3}	35.6

particles may be loosely bound at the edge of the gravitational influence of the planetesimal (i.e. near the Hill radius) or simply passing through the high-density grid cells that are identified as planetesimals. We will explore these ideas with velocity and vertical position data in Section 4.2. For the purposes of this analysis, we identify these transient clump particles as “lost”, and plot the composition of this lost dust mass in the bottom panel of Figure 7 and provide the time averages of these data in Table 2b. The lost dust mass is nearly evenly distributed among the grains at $\tau_s > 0.1$, with the highest proportion involving the $\tau_s = 0.270$ grains. Note that on average, approximately 10% of all the mass in clumps is consistently lost between snapshots.

We can combine the results from the two panels of Figure 7 into a single idea known as the residence time—a quantity that estimates how long the dust mass of a particular grain species will remain in clumps given how quickly that mass is lost. This is represented simply by,

$$\text{Residence time} = \Delta t_{\text{snap}} \left(\frac{\text{Mass in clumps}}{\text{Mass lost btwn. snapshots}} \right), \quad (18)$$

where Δt_{snap} is the amount of time between data outputs and in this study is equal to $2.0 \Omega^{-1}$. The residence time is hence equivalent to dividing the data in Table 2a by the data in Table 2b and multiplying by Δt_{snap} .

We present calculations of the residence time in Table 3. This

⁴ Planetesimals in concurrent simulation snapshots which share over 50%

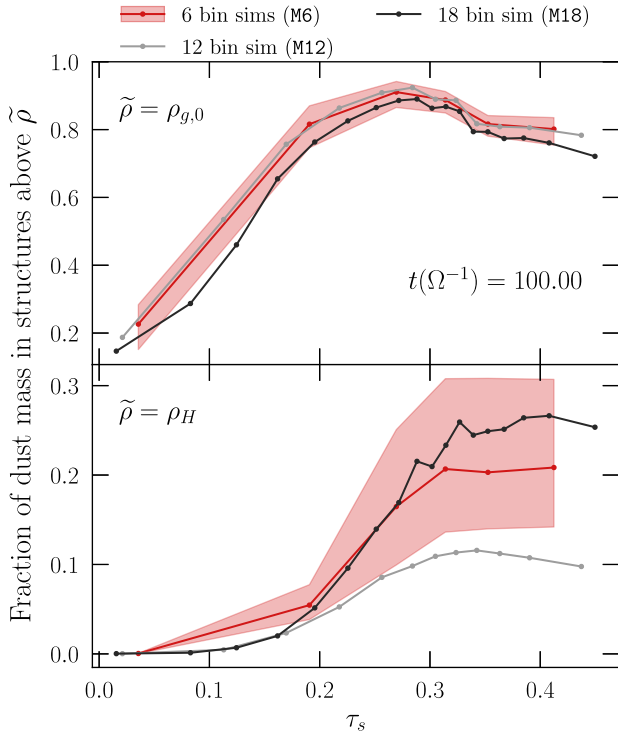


Figure 8. Total dust mass above certain density thresholds ($\tilde{\rho}$) as a function of grain size (τ_s), normalized by the total dust mass in each grain size bin. In the top panel the threshold is the initial midplane gas density $\rho_{g,0}$ and the bottom panel the threshold is the Hill density (equation 13), the threshold above which dust forms gravitationally bound planetesimals. The shaded regions represent the bound for the maximum and minimum across the five M6 simulations. The M12 and M18 data are shown with grey and black curves, with multiplications by 2 and 3 to allow for a direct comparison with the M6 simulations, which have fewer bins and hence more dust mass per bin.

table confirms our prior conclusions when considering both panels of Figure 7 together: the largest grains are the most bound, longest-lived components of the planetesimals. All grains with $\tau_s > 0.2$ have residence times above $18 \Omega^{-1}$, and this quantity increases monotonically with τ_s . The smallest grains at $\tau_s = 0.036$ have residence times comparable to Δt_{snap} , suggesting they form only a transient component of the clump mass⁵.

Interestingly, the $\tau_s = 0.191$ grains have an intermediate residence time of $\sim 8 \Omega^{-1}$. We can also observe from the dust surface density maps for each grain species (Fig. 2) and the PDF of those surface densities (top panel Fig. 4) that the $\tau_s = 0.191$ grains exhibit behavior that is not like the smallest grains or the larger grains. The smallest grains do not participate in any kind of dust clumping, and the larger grains readily form gravitationally unstable planetesimals. Our results suggest the $\tau_s = 0.191$ grain behavior is in-between these two regimes.

We can see evidence of this in-between behavior for the $\tau_s = 0.191$ grains in Figure 8, which shows the amount of dust mass above a certain density threshold at each grain size at $t = 100 \Omega^{-1}$. In the bottom panel, the threshold is ρ_H , and hence these data are

⁵ A more sophisticated clump-finding approach may definitely determine these small grains to be kinematically unbound. However, our simpler (and less expensive) analysis reaches the same conclusion to the degree of precision suitable for our study.

equivalent to (a single time/vertical slice of) the data from the top panel of Figure 7. We see similar conclusions as before: the $\tau_s > 0.2$ grains dominate the clump mass budget, the $\tau_s = 0.036$ grains are not a part of the clumps at all, and the $\tau_s = 0.191$ make up a small fraction of the mass at clump densities.

In the top panel of Figure 8, the threshold is $\rho_{g,0}$, the mid-plane gas density. In our simulations and those like it from the literature, the gas density displays little variation, even when the streaming instability develops strong dust clumps and filaments (Li et al. 2018). So the $\rho_{g,0}$ threshold effectively marks the boundary where the dust density dominates the total local mass density ($\rho = \rho_d + \rho_g$), an important regime for the streaming instability (Youdin & Goodman 2005). We see that the $\tau_s = 0.036$ grains are underrepresented, even at the lower threshold of $\rho_{g,0}$, representing $\sim 7\%$ of all dust mass. Meanwhile, the $\tau_s = 0.191$ grains contribute just as much mass above this threshold as the larger grains.

Including observations from the dust surface density at each grain size (Fig. 2), we can interpret the data in Figure 8 as supporting the idea that the $\tau_s = 0.191$ grains form filaments but not strong clumps, while the smaller $\tau_s = 0.036$ grains form neither. In other words, the $\rho_{g,0}$ threshold appears to delimit the dust density boundary for the filamentary features.

4.1 Simulations with larger numbers of species

As with the results from Section 3, using a larger number of grain species to sample the grain size distribution does not change our results. In Table 2, we include time averages of the mass in clumps and lost by clumps for the M12 and M18 simulations. As discussed in Section 2.2.2, the larger bin samples are created by sub-sampling the 6 bins from the M6 simulations, so that we can easily combine the sub-sampled bins to match the τ_s bin boundaries from 6 bin sample for the purposes of comparison. The overall conclusions from the M12 and M18 data are the same: the larger $\tau_s > 0.2$ grains dominate the clump mass budget, while the dust mass lost is more evenly spread among the $\tau_s > 0.1$ grains. Also, the shape of the curves from Figure 8 are within the bounds set by the M6 simulations.

We note that, as a whole, including Figure 5, the M12 has slightly lower mass in clumps and dense structures than the M6 average, while the M18 data is slightly above this average. We do not interpret these differences as evidence that an increased number of bins affects planetesimal formation in a deterministic way. Rather, we view these differences as a consequence of the non-linear nature of the developed stage of the streaming instability. The variability in the SI is immediately observable as the range of outcomes among the individual M6 and S simulations, and was the overarching theme of our previous study (Rucska & Wadsley 2021).

4.2 Dust velocity

In this section we use velocity data to further explore the differences in behavior between the smaller and larger dust grains in our simulations, and the consequences this has on planetesimal formation.

A 2D histogram of the dust particles in the dust volume density (ρ_d) and individual particle velocity ($|\mathbf{v}_{\text{dust}}|$) phase space, for the M6-0 run, is shown in Figure 9. Also plotted is the magnitude of the equilibrium drift velocity for the dust (Nakagawa et al. 1986) as the white curve, which tracks the expected steady-state drift rates of the dust (in the absence of complex dynamics like the non-linear SI). We see at large ρ_d , the expected drift velocity falls to 0, predicting that the dust fully decouples from the dust-gas equilibrium and orbits at

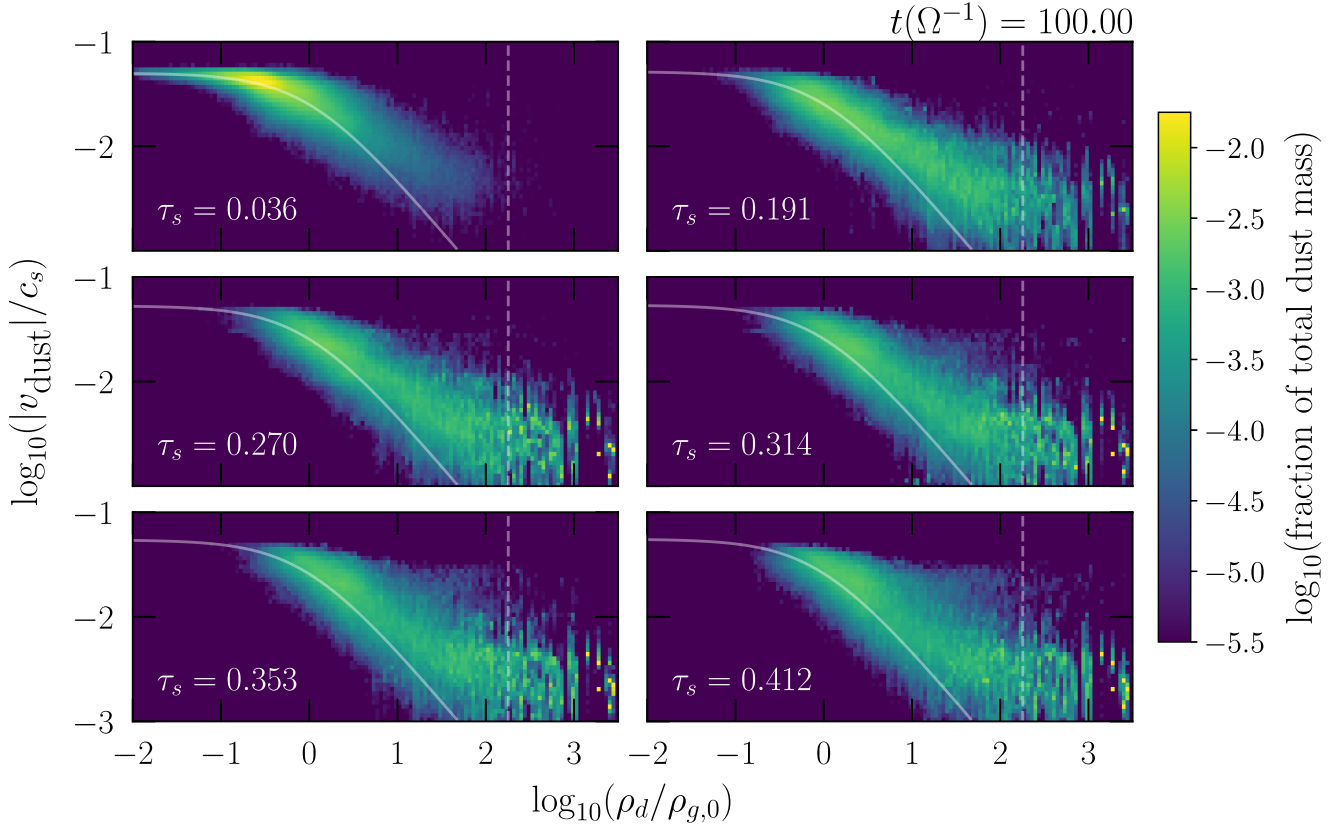


Figure 9. 2D histogram in the dust density-velocity phase space for the different grains in the M6-0 simulation at $t = 100\Omega^{-1}$. Each panel is the histogram for the individual grain species. Note that all dust velocities are measured with respect to the background Keplerian flow. The (logarithmic) colourbar is normalized to the total dust mass in the simulation. The darkest bins do not contain any particles; a minimum value is applied for aesthetic purposes. The solid white curve represents the NSH equilibrium velocity (Nakagawa et al. 1986; see also equations 7 in Youdin & Johansen 2007) and the vertical white dashed line represents the Hill density in our simulation units (equation 13). The NSH velocity is a function of τ_s and the local dust-to-gas mass ratio, $\epsilon = \rho_d/\rho_g$. Since $\rho_g \approx 1$ throughout our simulation domain, we use ρ_d as a proxy for ϵ .

the Keplerian velocity, and at low ρ_d the drift velocity approaches to the radial pressure gradient offset $\sim \eta v_K$ with a factor of order unity that depends on τ_s .

The smallest $\tau_s = 0.036$ dust grains have most of their mass below $\rho_{g,0}$, which is in line with conclusions regarding Figure 8. Nearly all of the dust at this size—which does not form filaments or clumps—follows the NSH equilibrium curve closely. This provides further evidence that these smallest grains do not participate in highly non-linear behavior that deviates from analytical, steady-state expectations.

Most of the $\tau_s = 0.191$ grains do not exist at densities above $\rho_H = 180$, but between 30 and $100\rho_{g,0}$, which corroborates earlier discussions in Section 4 which conclude these grains predominantly participate in filament formation but not clump formation. The lower density dust between ~ 0.3 and $10\rho_{g,0}$ primarily follows the NSH equilibrium curve.

For the larger $\tau_s > 0.2$ grains, most of their mass exists at large densities well above ρ_H . Dust in the centre of planetesimals can be seen as the bright yellow pixels at $\rho_d \geq 10\rho_H$. The lines of above and below these brightest pixels show that the dust resolution element superparticles can have slightly different velocities within a single grid cell. As with the $\tau_s = 0.191$ grains, the lower density dust is centered around the NSH expectations.

Note that for all grains with dust densities above $\sim 30\rho_{g,0}$, the bulk of the mass deviates substantially from the NSH equilib-

rium, settling at velocities between ~ 0.001 and $0.01c_s$. This is evidence of small amplitude, local turbulence, likely driven in part by the dense dust clumps near the midplane imparting substantial momentum onto the gas over small length scales. The width of the histogram about the NSH curve at lower densities is likely a result of this more disperse dust interacting with stirred up midplane gas.

4.3 Vertical position

We can further highlight the different behavior between the different sized dust grains by briefly exploring the properties of the vertical (out of midplane) dynamics. Figure 10 shows the dust surface density in the radial-vertical (x - z) plane. We can see that small grains have a much more extended vertical profile than any of the larger grains, with no bright features. Comparatively, the $\tau_s = 0.314$ grains (which look nearly identical to the other grains in the largest four sizes, which are not shown) are distributed very closely to the midplane. The $\tau_s = 0.191$ are slightly more extended with slightly broader features than the large grains, and the bright planetesimal between $x = 0.0$ and $0.05H_g$ is not very bright in these grains. Yet, the filament features are readily visible.

We can further quantify these observations by computing the

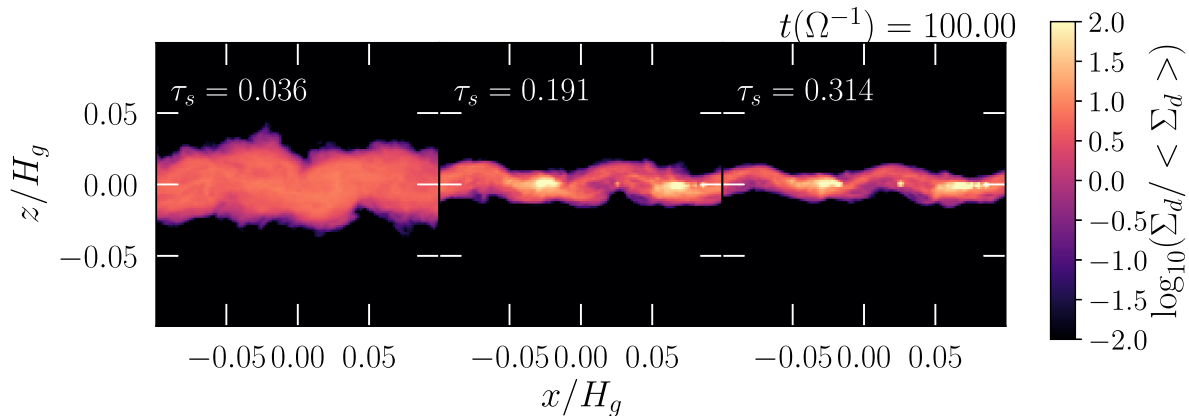


Figure 10. Dust surface density in the x - z (radial-vertical) plane for a subset of grains from the M6-0 simulation at $t = 100\Omega^{-1}$.

Table 4. Particle scale height and vertical RMS velocity for the different dust grains in the M6-0 simulation at $t = 100\Omega^{-1}$.

τ_s	H_p (H_g)	$v_{z,\text{rms}}$ (c_s)
0.036	11.7×10^{-3}	4.16×10^{-3}
0.191	4.47×10^{-3}	2.87×10^{-3}
0.270	3.40×10^{-3}	2.50×10^{-3}
0.314	3.03×10^{-3}	2.31×10^{-3}
0.353	2.77×10^{-3}	2.29×10^{-3}
0.412	2.64×10^{-3}	2.37×10^{-3}

dust scale height, defined as,

$$H_p = \sqrt{\frac{1}{N_{\text{par}}} \sum_i^{N_{\text{par}}} (z_i - \bar{z})^2}, \quad (19)$$

and a similar (and related) quantity, the root mean-square (RMS) z velocity,

$$v_{z,\text{rms}} = \sqrt{\frac{1}{N_{\text{par}}} \sum_i^{N_{\text{par}}} (v_{z,i} - \bar{v}_z)^2}. \quad (20)$$

These values for all dust grains in the M6-0 simulation are presented in Table 4. The H_p data confirm what is visible in the vertical surface density: the smallest grains have by far the most vertically extended scale heights, and the scale height monotonically decreases with τ_s . The scale height is directly related to the RMS of the vertical dust velocity since it is only through turbulent motions—which provide a constant source of vertical velocity dispersion—that the dust can maintain a persistent scale height (Youdin & Lithwick 2007). Similar to observations made by Schaffer et al. (2018, 2021) in their 2D simulations of the SI with multiple grains, it appears in our simulations that the larger grains stir up turbulence near the midplane, which causes the smaller grains, which are more tightly coupled to the gas aerodynamically (short drag stopping times), to remain suspended at relatively large scale heights. The vertical RMS velocity for the gas near the midplane is 4.13×10^{-3} (in units of c_s), which is very close to $v_{z,\text{rms}}$ for the small $\tau_s = 0.036$ grains.

5 CONCLUSIONS AND DISCUSSION

In this study we model a patch of a protoplanetary disc in 3D numerical hydrodynamics simulations. We model the dust component of

the disc with multiple grain sizes simultaneously under conditions that are unstable to the streaming instability, and track the non-linear development of the SI to the formation of bound planetesimals. This paper extends previous work that used multiple grain sizes in simulations of the non-linear phase of the SI (Johansen et al. 2007; Bai & Stone 2010b; Schaffer et al. 2018, 2021; Yang & Zhu 2021). Most prior work used a grain size distribution with a number density described by a single power law, but in our study we sample a distribution that is the output of a widely-used model of grain growth and fragmentation applicable to midplane of protoplanetary discs (Birnstiel et al. 2011). To compare our multi-species results to prior work which modelled the dust with a single species, we match the peak of the size distribution to the grain size studied in Rucska & Wadsley (2021).

Our main results are as follows:

(i) Only larger grains with dimensionless stopping times $\tau_s > 0.1$ participate strongly in the non-linear SI, producing filaments and regions with large dust densities that gravitationally collapse into planetesimals. The smaller grains do not form filaments or clumps at all, despite the fact they are embedded in an environment where roughly 5/6 of the dust mass is forming dense structures. This confirms a basic property of the multi-species SI at the non-linear stage (Bai & Stone 2010b; Yang & Zhu 2021), which remains true for a realistic protoplanetary disc grain size distribution from Birnstiel et al. (2011). The net result is there is more dust mass in the regions between the filaments in the multi-species simulations when compared to the single grain simulations, and slightly less mass in the dense structures.

(ii) Clumping of dust via the SI on sub-AU length scales reduces the average surface brightness for a given amount of dust. This confirms in 3D models that the SI may explain the lower than expected (order unity) optical depths inferred in observed protoplanetary disc rings (see Section 3.1 for details). We estimate that 20%-80% more dust may be present than in uniform mass distribution models. The effect is less severe for multi-size versus single-size models.

(iii) We identify bound clumps and dense dust features. Larger $\tau_s \gtrsim 0.2$ grains form clumps, $\tau_s \lesssim 0.04$ grains do not form clumps or filaments. Intermediate sizes are somewhat in between, forming filaments but not clumps. The velocities of the smallest grains are quite different from the larger grains in clumps and filaments, suggesting that these small grains—with a short drag stopping time that enforces tight coupling to the gas—simply sweep by the planetes-

imals rather than becoming incorporated into them. This implies a lower size cutoff for pebble and dust grains incorporated into asteroids and comets.

(iv) The main group of the multi-species runs in this study used 6 bins or species to sample of the grain size distribution. We test 12 and 18 bins to show convergence. More bins appears to have no appreciable effect on the results for the multi-species simulations and we conclude that 6 bins is sufficient to study peaked grain size distributions.

5.1 The future of planetesimal formation via the SI with multiple grain sizes

Including multiple sizes in models of the non-linear SI affects not just planetesimal formation but also the observable properties of protoplanetary discs. Most prior work on the SI has modelled the dust with a single grain size. However, recent observations of protoplanetary discs (see [Andrews 2020](#), for a review) and results from grain growth theory ([Birnstiel et al. 2011, 2015](#)) suggest that there is a distribution of dust grain sizes within discs. An important consideration then is what the shape of this distribution should be.

In this paper we have shown that just an order of magnitude difference in grain size can determine whether grains are fully active in the SI all the way to planetesimal formation, or whether they do not even form filaments. This result motivates further exploration of the grain size distribution parameter space. Our study represents a single instance of the [Birnstiel et al. \(2011\)](#) distribution for a specific set of disc conditions. In our results, most of the species participate in planetesimal formation. Shifting the distribution peak to smaller sizes—equivalent to considering different radial positions in the disc—would move dust mass from species that undergo strong clumping towards species that do not participate in planetesimal formation or primarily form only filaments. Presumably, this would result in an overall decrease in the total dust mass that is converted to planetesimals and may act to suppress the instability itself. Extending our work to a broader range of distributions would reveal how planetesimal formation varies in conditions at different radial locations in the disc.

Of particular interest is a distribution with a more equal mix of SI-active and SI-inactive grains. These conditions likely describe the onset of the SI and planetesimal formation. Early in the disc lifetime, most of the dust in the midplane may be too small ($\tau_s \lesssim 0.04$) to participate in planetesimal formation initially, and then grow through mutual collisions (e.g. [Birnstiel et al. 2011](#)) to involve sizes that are unstable to the SI. However, the time scales for grain growth are typically $> 10^4$ yr (e.g. [Birnstiel et al. 2012](#)), while the timescale for planetesimal formation via the SI is much shorter⁶. Thus, for initially small grains, planetesimal formation may occur as grains grow. It would be interesting to explore this initial planetesimal formation phase with a dust size distribution that includes a larger proportion of smaller, SI-inactive grains.

More realistically, however, it is likely grain growth and the streaming instability occur simultaneously. Dust growth and fragmentation is driven by collisions between dust grains. The source of the relative velocity for these collisions in models such as [Birnstiel et al. \(2011\)](#) is an underlying turbulence that may be driven by large scale hydrodynamic instabilities (see [Lyra & Umurhan](#)

[2019](#), for a review). The streaming instability generates its own turbulence locally (e.g. [Li et al. 2018](#)) that drives relative velocities between dust, especially when a distribution of sizes is considered ([Bai & Stone 2010b](#)). How these SI-driven collisions influence grain growth remains unstudied. A possible technique may be a model where the dust size can change based on collisions and expectations of growth/fragmentation. These dynamic grain size models have been applied to global models of disc evolution (e.g. [Gonzalez et al. 2017; Drążkowska et al. 2021](#)), yet have not appeared in high resolution studies of the SI.

Our results show that, under the SI, a distribution of sizes will segregate spatially. The larger, pebble-sized dust settles to the midplane and undergoes vigorous non-linear dynamics leading to filament and planetesimal formation, while the smaller grains remain vertically suspended and occupy the space between filaments. Thus, the influence of grain growth likely varies spatially as well. Perhaps the small, vertically suspended grains could grow to sizes that are more SI-active, settle towards the midplane, and participate in planetesimal formation. The dense, dust-dominated regions within filaments could promote the growth of pebbles to larger sizes than is possible in gas-dominated regimes. Or, the pebbles in filaments could fragment to smaller SI-inactive grains and reduce the efficiency of planetesimal formation. These smaller sized, fragmented remnants would be created at low scale heights near the midplane, and it is unclear how those grains would interact with clumps and pebble-rich filaments. Such possibilities could be explored in dynamic grain size models.

Incorporating grain growth introduces models dependent on physical units (e.g. fragmentation threshold velocity). This breaks the scale-free property of the common shearing box model used in high-resolution studies of the SI that allows, for example, the translation of $\tau_s = 0.314$ dust to represent different physical grain sizes depending on the disc model and radial position. This means multiple simulations will be required to model how grain growth theory interacts with the local dynamics of the streaming instability under different disc conditions.

The composition of grains could also influence both grain growth and the aerodynamic coupling between the solids and gas phase. Icy grains can stick together at larger collisional velocities than silicate grains (e.g. [Gundlach & Blum 2015](#)), and since icy grains are, generally speaking, larger than dry grains, they can radially drift through protoplanetary discs at different rates ([Drążkowska & Alibert 2017](#)). If both dry and icy grains co-exist in a disc region that is unstable to the SI (in the vicinity of a disc ice line), our results suggest the two populations could become spatially separated. The small, dry grains would preferentially remain suspended above the disc midplane while the larger, SI-active icy grains would form filaments and planetesimals. This would distinguish the chemical composition of the planetesimals from the overall dust population within which they are formed.

Improving numerical resolution to near planetesimal (~ 10 km) length scales could confirm our interpretation of our results that small grains do not participate in clump formation because they are tightly coupled to the gas which flows around the planetesimals. An increase in resolution to this scale is not possible with the methods applied to the streaming instability thus far, but may be approachable with adaptive resolution techniques and/or zoom-in simulations with small domains.

The ability of the available numerical schemes to model an aerodynamically coupled solids-gas system with a dynamic grain size distribution also remains unexplored. [Bai & Stone \(2010b\)](#) suggested that 1 dust superparticle per grid cell per grain species

⁶ For the timescales in our study, $100\Omega^{-1} \approx 16$ orbital periods, which is equivalent to ~ 200 years at 5 AU around a solar mass star.

is adequate to capture the non-linear SI, and this has been the literature standard since. It is unclear how this would translate to a dust phase with a continuous, dynamic size range. Difficulties and uncertainties aside, we believe a dynamic dust size distribution could be a promising avenue for approaching a more realistic model of planetesimal formation via the streaming instability.

ACKNOWLEDGEMENTS

These simulations were performed on the Niagara supercomputing cluster operated by SciNet and Compute Canada. JW thanks NSERC for funding support.

DATA AVAILABILITY

The data underlying this article will be shared on reasonable request to the corresponding author.

REFERENCES

- Abod C. P., Simon J. B., Li R., Armitage P. J., Youdin A. N., Kretke K. A., 2019, *ApJ*, **883**, 192
- Andrews S. M., 2020, *ARA&A*, **58**, 483
- Andrews S. M., et al., 2016, *ApJ*, **820**, L40
- Armitage P. J., 2020, *Astrophysics of Planet Formation*, 2 edn. Cambridge Univ. Press
- Avenhaus H., et al., 2018, *ApJ*, **863**, 44
- Bai X.-N., Stone J. M., 2010a, *ApJS*, **190**, 297
- Bai X.-N., Stone J. M., 2010b, *ApJ*, **722**, 1437
- Benisty M., et al., 2015, *A&A*, **578**, L6
- Benisty M., et al., 2017, *A&A*, **597**, A42
- Birnstiel T., Ormel C. W., Dullemond C. P., 2011, *A&A*, **525**, A11
- Birnstiel T., Klahr H., Ercolano B., 2012, *A&A*, **539**, A148
- Birnstiel T., Andrews S. M., Pinilla P., Kama M., 2015, *ApJ*, **813**, L14
- Birnstiel T., Fang M., Johansen A., 2016, *Space Sci. Rev.*, **205**, 41
- Birnstiel T., et al., 2018, *ApJ*, **869**, L45
- Blum J., et al., 2017, *MNRAS*, **469**, S755
- Carrera D., Simon J. B., 2022, *ApJ*, **933**, L10
- Carrera D., Johansen A., Davies M. B., 2015, *A&A*, **579**, A43
- Carrera D., Simon J. B., Li R., Kretke K. A., Klahr H., 2021, *AJ*, **161**, 96
- Carrera D., Thomas A. J., Simon J. B., Small M. A., Kretke K. A., Klahr H., 2022, *ApJ*, **927**, 52
- Cazzoletti P., et al., 2018, *A&A*, **619**, A161
- Chiang E. I., Goldreich P., 1997, *ApJ*, **490**, 368
- Drążkowska J., Alibert Y., 2017, *A&A*, **608**, A92
- Drążkowska J., Stammer S. M., Birnstiel T., 2021, *A&A*, **647**, A15
- Dullemond C. P., et al., 2018, *ApJ*, **869**, L46
- Epstein P. S., 1924, *Phys. Rev.*, **23**, 710
- Franceschi R., Birnstiel T., Henning T., Sharma A., 2023, *A&A*, **671**, A125
- Fulle M., Blum J., 2017, *MNRAS*, **469**, S39
- Goldreich P., Lynden-Bell D., 1965, *MNRAS*, **130**, 125
- Gole D. A., Simon J. B., Li R., Youdin A. N., Armitage P. J., 2020, arXiv e-prints, [p. arXiv:2001.10000](https://arxiv.org/abs/2001.10000)
- Gonzalez J. F., Laibe G., Maddison S. T., 2017, *MNRAS*, **467**, 1984
- Grishin E., Malamud U., Perets H. B., Wand el O., Schäfer C. M., 2020, *Nature*, **580**, 463
- Gundlach B., Blum J., 2015, *ApJ*, **798**, 34
- Güttler C., Blum J., Zsom A., Ormel C. W., Dullemond C. P., 2010, *A&A*, **513**, A56
- Hawley J. F., Gammie C. F., Balbus S. A., 1995, *ApJ*, **440**, 742
- Hayashi C., 1981, *Progress of Theoretical Physics Supplement*, **70**, 35
- Huang J., et al., 2018, *ApJ*, **869**, L42
- Johansen A., Youdin A., 2007, *ApJ*, **662**, 627

- Johansen A., Oishi J. S., Mac Low M.-M., Klahr H., Henning T., Youdin A., 2007, *Nature*, **448**, 1022
- Johansen A., Youdin A., Mac Low M.-M., 2009, *ApJ*, **704**, L75
- Johansen A., Youdin A. N., Lithwick Y., 2012, *A&A*, **537**, A125
- Johansen A., Mac Low M.-M., Lacerda P., Bizzarro M., 2015, *Science Advances*, **1**, 1500109
- Johnson B. M., Guan X., Gammie C. F., 2008, *ApJS*, **179**, 553
- Kavelaars J. J., Petit J.-M., Gladman B., Bannister M. T., Alexandersen M., Chen Y.-T., Gwyn S. D. J., Volk K., 2021, *ApJ*, **920**, L28
- Kim C.-G., Ostriker E. C., 2017, *ApJ*, **846**, 133
- Krapp L., Benítez-Llambay P., Gressel O., Pessah M. E., 2019, *ApJ*, **878**, L30
- Li R., Youdin A. N., 2021, *ApJ*, **919**, 107
- Li R., Youdin A. N., Simon J. B., 2018, *ApJ*, **862**, 14
- Li R., Youdin A. N., Simon J. B., 2019, *ApJ*, **885**, 69
- Lyra W., Umurhan O. M., 2019, *PASP*, **131**, 072001
- Macías E., et al., 2019, *ApJ*, **881**, 159
- Marohnic J. C., et al., 2021, *Icarus*, **356**, 113824
- Masset F., 2000, *A&AS*, **141**, 165
- Mathis J. S., Rumpl W., Nordsieck K. H., 1977, *ApJ*, **217**, 425
- Maucó K., et al., 2021, *ApJ*, **923**, 128
- McKinnon W. B., et al., 2020, *Science*, **367**, aay6620
- McNally C. P., Lovascio F., Paardekoooper S.-J., 2021, *MNRAS*, **502**, 1469
- Moore G. S. M., Rose H. E., 1973, *Nature*, **242**, 187
- Muto T., et al., 2012, *ApJ*, **748**, L22
- Nakagawa Y., Sekiya M., Hayashi C., 1986, *Icarus*, **67**, 375
- Nesvorný D., Li R., Youdin A. N., Simon J. B., Grundy W. M., 2019, *Nature Astronomy*, **3**, 808
- Nesvorný D., Li R., Simon J. B., Youdin A. N., Richardson D. C., Marshall R., Grundy W. M., 2021, *PSJ*, **2**, 27
- Paardekooper S.-J., McNally C. P., Lovascio F., 2020, *MNRAS*, **499**, 4223
- Paardekooper S.-J., McNally C. P., Lovascio F., 2021, *MNRAS*, **502**, 1579
- Pérez L. M., et al., 2016, *Science*, **353**, 1519
- Robbins S. J., Singer K. N., 2021, *PSJ*, **2**, 192
- Robbins S. J., et al., 2017, *Icarus*, **287**, 187
- Rucsa J. J., Wadsley J. W., 2021, *MNRAS*, **500**, 520
- Scardoni C. E., Booth R. A., Clarke C. J., 2021, *MNRAS*, **504**, 1495
- Schäfer U., Yang C.-C., Johansen A., 2017, *A&A*, **597**, A69
- Schaffer N., Yang C.-C., Johansen A., 2018, *A&A*, **618**, A75
- Schaffer N., Johansen A., Lambrechts M., 2021, *A&A*, **653**, A14
- Shakura N. I., Sunyaev R. A., 1973, *A&A*, **24**, 337
- Simon J. B., Armitage P. J., Li R., Youdin A. N., 2016, *ApJ*, **822**, 55
- Simon J. B., Armitage P. J., Youdin A. N., Li R., 2017, *ApJ*, **847**, L12
- Singer K. N., et al., 2019, *Science*, **363**, 955
- Squire J., Hopkins P. F., 2018, *MNRAS*, **477**, 5011
- Squire J., Hopkins P. F., 2020, arXiv e-prints, [p. arXiv:2003.01738](https://arxiv.org/abs/2003.01738)
- Stammler S. M., Drążkowska J., Birnstiel T., Klahr H., Dullemond C. P., Andrews S. M., 2019, *ApJ*, **884**, L5
- Stone J. M., Gardiner T., 2009, *New Astron.*, **14**, 139
- Stone J. M., Gardiner T. A., 2010, *ApJS*, **189**, 142
- Stone J. M., Gardiner T. A., Teuben P., Hawley J. F., Simon J. B., 2008, *ApJS*, **178**, 137
- Toomre A., 1964, *ApJ*, **139**, 1217
- Walsh K. J., 2018, *ARA&A*, **56**, 593
- Weidenschilling S. J., 1977a, *Ap&SS*, **51**, 153
- Weidenschilling S. J., 1977b, *MNRAS*, **180**, 57
- Whipple F. L., 1972, in Elvius A., ed., *From Plasma to Planet*. p. 211
- Windmark F., Birnstiel T., Güttler C., Blum J., Dullemond C. P., Henning T., 2012, *A&A*, **540**, A73
- Xu Z., Bai X.-N., 2022a, arXiv e-prints, [p. arXiv:2207.08858](https://arxiv.org/abs/2207.08858)
- Xu Z., Bai X.-N., 2022b, *ApJ*, **924**, 3
- Yang C.-C., Zhu Z., 2021, *MNRAS*, **508**, 5538
- Yang C.-C., Johansen A., Carrera D., 2017, *A&A*, **606**, A80
- Youdin A., Goodman J., 2005, *ApJ*, **620**, 459
- Youdin A., Johansen A., 2007, *ApJ*, **662**, 613
- Youdin A. N., Lithwick Y., 2007, *Icarus*, **192**, 588
- Zhu Z., Yang C.-C., 2021, *MNRAS*, **501**, 467

Zsom A., Ormel C. W., Güttler C., Blum J., Dullemond C. P., 2010, [A&A](#),
[513](#), [A57](#)
van der Marel N., et al., 2013, [Science](#), [340](#), [1199](#)
van der Marel N., Pinilla P., Tobin J., van Kempen T., Andrews S., Ricci L.,
Birnstiel T., 2015, [ApJ](#), [810](#), [L7](#)
van der Marel N., et al., 2021, [AJ](#), [161](#), [33](#)

This paper has been typeset from a $\text{\TeX}/\text{\LaTeX}$ file prepared by the author.